

PAPER

[View Article Online](#)
[View Journal](#) | [View Issue](#)Cite this: *Mater. Adv.*, 2022,
3, 7348Exploring the effect of partial B-site Al^{3+} – Mg^{2+}
dual substitution on optoelectronic, surface,
and photocatalytic properties of $\text{BaTaO}_2\text{N}^\dagger$ Mirabbos Hojamberdiev, ^{*ab} Ronald Vargas, ^{cd} Zukhra C. Kadirova,^{ef}
Katsuya Teshima ^{bg} and Martin Lerch^a

BaTaO_2N is appraised to be one of the few promising 600 nm-class photocatalysts for solar water splitting. However, the presence of structural defects and low charge separation limits its photocatalytic activity. Compared with mono substitution, dual substitution can be more effective in engineering the structural defects and improving the photocatalytic activity if foreign ions are suitably selected. In this work, we involve a dual-substitution approach to partially substitute Al^{3+} and/or Mg^{2+} for Ta^{5+} in BaTaO_2N . By maintaining the maximum concentration of Al^{3+} – Mg^{2+} dual substitution at 5%, the effect of the Al^{3+} – Mg^{2+} cosubstituent ratio on the optoelectronic, surface, and photocatalytic properties of BaTaO_2N is investigated. The Al^{3+} – Mg^{2+} dual substitution leads to the shift of optical absorption edge toward shorter wavelengths, increasing the optical bandgap energy of BaTaO_2N . This effect is more pronounced in the samples with a higher concentration of Mg^{2+} due to the replacement of N^{3-} by a large number of O^{2-} to compensate charge balance. The initial reaction rates for the evolution of O_2 and H_2 reveal the improvement in the photocatalytic activity of BaTaO_2N due to the partial Al^{3+} – Mg^{2+} dual substitution. Higher O_2 evolution is observed in the samples with a higher concentration of Mg^{2+} , while the H_2 evolution rate significantly relies on the increased concentration of Al^{3+} . According to the density functional theory (DFT) calculations, the effective masses of electrons become slightly lower than that of pristine BaTaO_2N after partial Al^{3+} – Mg^{2+} (co)substitution, while a contrary tendency is observed for the effective masses of holes. The calculated positions of the valence band maximum and conduction band minimum are aligned with respect to the normal hydrogen electrode (NHE), and partial Al^{3+} – Mg^{2+} (co)substituted BaTaO_2N photocatalysts can be promising candidates for visible-light-induced water splitting.

Received 30th May 2022,
Accepted 3rd August 2022

DOI: 10.1039/d2ma00611a

rsc.li/materials-advances

1. Introduction

As a carbon-free chemical process to generate green hydrogen, solar water splitting depends on various important photochemical and photophysical properties of photocatalytic materials. Particularly, band structure, optical absorption, charge density, charge mobility, charge separation, defect density, surface structure, particle size, crystallinity, etc. can be modulated by (co)substituting cations and anions in the crystal structures of host photocatalytic materials by foreign ions to improve their solar water-splitting efficiency.^{1,2}

Many efforts have so far been made to enhance the water-splitting efficiency of various oxide and non-oxide photocatalytic materials by a cosubstitution. For instance, an apparent quantum yield (AQY) of 3.2% under visible light (420–800 nm) was reached by partial substitution of In^{3+} for Bi^{3+} and Mo^{6+} for V^{5+} in the host lattice of scheelite $m\text{-BiVO}_4$ due to uplifting the conduction band edge position above the proton reduction potential ($0 V_{\text{RHE}}$ at

^a Institut für Chemie, Technische Universität Berlin, Straße des 17. Juni 135, 10623 Berlin, Germany. E-mail: khujaamberdiev@tu-berlin.de, hmirabbos@gmail.com^b Department of Materials Chemistry, Shinshu University, Nagano 380-8553, Japan^c Instituto Tecnológico de Chascomús (INTECH) – Consejo Nacional de Investigaciones Científicas y Técnicas (CONICET)/Universidad Nacional de San Martín (UNSAM), Avenida Intendente Marino, Km 8,2, (B7130IWA), Chascomús, Provincia de Buenos Aires, Argentina^d Escuela de Bio y Nanotecnologías, Universidad Nacional de San Martín (UNSAM), Avenida Intendente Marino, Km 8,2, (B7130IWA), Chascomús, Provincia de Buenos Aires, Argentina^e Department of Inorganic Chemistry, National University of Uzbekistan, 100174 Tashkent, Uzbekistan^f Uzbekistan-Japan Innovation Center of Youth, University Street 2B, 100095 Tashkent, Uzbekistan^g Research Initiative for Supra-Materials, Shinshu University, 4-17-1 Wakasato, Nagano 380-8553, Japan[†] Electronic supplementary information (ESI) available. See DOI: <https://doi.org/10.1039/d2ma00611a>

pH = 7).³ Compared with pristine BiVO₄, 0.5W–2Mo–BiVO₄ exhibited a significant increase in the donor concentration ($N_D = 1.03 \times 10^{28} \text{ m}^{-3}$), lifetime ($\tau_D = 3.8 \text{ s}$), and incident photon conversion efficiency (IPCE = 41%), a decrease in the flat band potential ($V_{fb} = 0.35 V_{RHE}$) and space charge layer thickness, and nearly ten times higher H₂ evolution.⁴ A photocurrent density of 1.97 mA cm^{-2} at $1.23 V_{RHE}$ and a relatively low onset potential of $0.68 V_{RHE}$ were obtained by a simultaneous introduction of Sn and Mo in $\alpha\text{-Fe}_2\text{O}_3$, where the former accelerated charge separation by improving conductivity and the latter induced high density of surface trapping states, leading to the inhibition of charge recombination kinetics in surface states.⁵ A significant increase in the concentration of (co)doped ions decreases the efficiency. By applying a computational method, Smart *et al.*⁶ recently found a doping clustering, which traps free-electron polarons and severely lowers the carrier concentration with respect to the doping concentration, to be responsible for the doping bottleneck in $\alpha\text{-Fe}_2\text{O}_3$, and proposed a codoping with dopants having low binding energies for clustering, such as Sn–Ti, as a solution. The formation of oxygen vacancies in SrTiO₃, which act as electron–hole recombination centers, was suppressed by Rh–La⁷ and La–Al⁸ codoping, resulting in apparent quantum yields of 1.1% at 420 nm and 78.43% under 365 nm, respectively. Layered perovskite Sr₂TiO₄ was activated by La/N codoping, using 0.5 wt% Rh/Cr₂O₃ as a cocatalyst, for overall water splitting under visible light due to the contribution of N and La for uplifting the valence band edge position and charge balancing, respectively.⁹ Wide-band-gap photocatalysts, such as NaTaO₃,¹⁰ BaTa₂O₆,¹¹ and KTaO₃,¹² were activated for H₂ evolution under visible light irradiation by introducing the Ir/La codopants. Along with La as a charge balancer, doped Ir could form relatively shallow impurity levels, and the H₂ evolution could proceed by electron transition from the impurity levels formed by Ir³⁺ to the conduction band. A negative shift in the onset potential of photoelectrochemical water splitting from about $0.8 V_{RHE}$ (for pristine Ta₃N₅) to $0.55 V_{RHE}$ under AM 1.5 G-simulated sunlight was observed for a Mg–Zr cosubstituted Ta₃N₅ photoanode because of the change in the bandgap potential.¹³ Very recently, Mg–Zr-codoped single-crystalline Ta₃N₅ exhibited 45-times greater photocatalytic water-reduction activity than undoped Ta₃N₅ and an outstanding apparent quantum yield (AQY) of 0.54% at 420 nm during the photocatalytic H₂ evolution reaction due to the simultaneously well-regulated defect species and surface properties.¹⁴

As a promising candidate for visible-light-driven water splitting because of its excellent visible light absorption up to 660 nm, narrow band gap, sufficient valence band potential for water oxidation, good stability, and nontoxicity,¹⁵ perovskite BaTaO₂N has gained significant research interest. Apparent quantum yields (AQY) of 0.06%,¹⁶ 2.1%,¹⁷ 6.8%,¹⁸ and 11.9%¹⁹ at 420 nm were progressively achieved for photocatalytic H₂ and O₂ evolution over BaTaO₂N, respectively, and an incident photon-to-current efficiency of $\approx 43\%$ at $1.23 V_{RHE}$ was obtained in photoelectrochemical water oxidation over BaTaO₂N.²⁰ In addition to other important strategies applied, such as flux growth,²¹ particle morphology- and size-controlled synthesis,²² time-retrenched synthesis,²³ thin-film fabrication,²⁴

facet-controlled synthesis,^{25,26} solid-solution,^{16,27} surface modification,¹⁹ tensile uniaxial strain,²⁸ and particle transfer method,²⁹ the A-site or B-site substitution or partial substitution of atoms with different radii or valences have been proven to be effective in tailoring the surface local structure and anion ordering and modulating the optical, electronic, surface, and photocatalytic properties of BaTaO₂N without altering its perovskite structure. Substituents with different valences act as either electron donors or acceptors and change the carrier concentration when introduced into the host lattice.³⁰ Although divalent (Mg²⁺, Ca²⁺, Sr²⁺, and Zn²⁺), trivalent (Al³⁺, Ga³⁺, and Sc³⁺), tetravalent (Ti⁴⁺ and Zr⁴⁺), and hexavalent (Mo⁶⁺ and W⁶⁺) cations were singly introduced into the BaTaO₂N lattice to improve its photocatalytic and photoelectrochemical water splitting efficiency,^{17,28,31–35} a dual-substitution effect on water splitting efficiency of BaTaO₂N has not been explored yet.

Many outstanding works, including the above-mentioned ones, on the enhancement of water splitting efficiency of various photocatalytic materials by a dual substitution and our recent work,³² where 5% Mg²⁺ and 5% Al³⁺ independently promoted the photocatalytic sacrificial O₂ and H₂ evolution over BaTaO₂N under visible light, respectively, inspired us to further explore the impact of a partial dual substitution on water splitting efficiency of BaTaO₂N. In this study, by maintaining the maximum concentration of partial Al³⁺–Mg²⁺ dual substitution at 5%, the effect of the Al³⁺–Mg²⁺ cosubstituent ratio on the optoelectronic, surface, and photocatalytic properties of BaTaO₂N is studied. By linking the materials characterization results to the evaluated photocatalytic activity, the contribution of the partial Al³⁺–Mg²⁺ dual substitution is discussed and insights into the possible underlying mechanisms are gained.

2. Experimental

2.1. Synthesis

Pristine and Al³⁺–Mg²⁺ cosubstituted BaTaO₂N powders were synthesized by a solid-state reaction route. BaCO₃ (99.99%, chemPUR), Ta₂O₅ (99%, Alfa Aesar), and Al₂O₃ (99.99%, Merck) or MgCO₃ (>99%, Merck) as cosubstituent sources were first mixed manually in a stoichiometric ratio. Then, the well-homogenized mixture was placed in a platinum crucible, heated at 950 °C for 6 h using a localized NH₃ delivery system (12.5 L h^{-1}), with a heating rate of 500 °C h^{-1} and a natural cooling rate. The synthesized BaTaO₂N (BTON) powders: with no substituent, 5% Al³⁺, 5% Mg²⁺, 2.5% Al³⁺ + 2.5% Mg²⁺, 3.5% Al³⁺ + 1.5% Mg²⁺, and 1.5% Al³⁺ + 3.5% Mg²⁺ were labeled as BTON1, BTON2, BTON3, BTON4, BTON5, and BTON6, respectively.

2.2. Characterization

The crystal structure was determined by X-ray diffraction (XRD; PANalytical X'Pert PRO) analysis using Cu-K_α radiation (Bragg–Brentano geometry). The microstructure was examined by scanning electron microscopy (SEM; GeminiSEM 500 NanoVP, Carl Zeiss). The elemental content was analyzed by



means of energy-dispersive X-ray spectroscopy (EDX; DSM 982 GEMINI, Carl Zeiss, with a Bruker Quantax XFlash[®] 6|60) and inductively coupled plasma-optical emission spectrometry (SPS5510, SII Nanotechnology Inc.). The UV-Vis diffuse reflectance spectra were measured using an Evolution 220 UV/Vis spectrometer (Thermo Fisher Scientific). The surface chemical composition and states of elements were analyzed using a PHI Quantera II scanning X-ray photoelectron microprobe (XPS; ULVAC-PHI, Inc.) with monochromatic Al-K_α radiation. The XPS profiles were fitted using a Gaussian-Lorentzian function, and the peak positions were normalized by positioning the C 1s peak at 284.5 eV.

2.3. Photocatalytic activity tests

The photocatalytic activity of pristine and (co)substituted BaTaO₂N samples was evaluated by comparing their H₂ and O₂ evolution promoted by Pt (0.5 wt%) and CoO_x (2 wt% Co) cocatalysts, respectively. The cocatalysts were loaded according to the processes reported elsewhere.³² The H₂ and O₂ evolution half-reactions were separately carried out in a Pyrex[®] side-irradiation-type reactor connected to a closed gas circulation and evacuation system. A 300 W Xe arc lamp (Cermex-PE300BF, PerkinElmer) with a UV-cutoff filter (L42, HOYA) and a cold mirror (CM-1, Optline) was used as the visible-light source, and the irradiance of visible light was 200 mW cm⁻². The quantity of evolved gases was analyzed by using a gas chromatograph (GC-8A, TCD, Ar gas carrier, Shimadzu), which was directly connected to the reactor. For the O₂-evolution half-reaction, 100 mg of CoO_x-loaded photocatalyst, 300 mL of 10 mM AgNO₃ (sacrificial electron scavenger), and 200 mg of La₂O₃ (pH buffer) were used, while 100 mg of Pt-loaded photocatalyst and 300 mL of 10 vol% aqueous methanol solution were used for the H₂-evolution half-reaction.

2.4. Computational methods

Density functional theory (DFT) simulations were performed within *Vienna ab initio simulation package* (VASP)^{36,37} in the projector augmented waves (PAW) scheme. The pristine BaTaO₂N cell (*Pm3̄m* space group, No. 221, *Z* = 1) was created based on the experimental structural data.³⁸ Several types of substitution have been considered in the present work. A 2 × 1 × 1 supercell was used to simulate a 50 at% substitution content of Al or Mg, *i.e.*, one substituent atom was substituted for Ta atom within the 10-atomic supercell. To model the cosubstitution contents of 25 at% Al and 25 at% Mg, one Al and one Mg atom were substituted for two Ta atoms within the 20-atomic 2 × 2 × 1 supercell. Simulation of 50 at% substitution, where one quarter is Al and three quarters is Mg, and *vice versa* were modeled within a 2 × 2 × 2 supercell with 40 atoms. All simulated configurations with the corresponding chemical compositions are listed in Table S1 (ESI[†]). The generalized gradient approximation (GGA) of the exchange-correlation potential in the PBE form³⁹ was adopted during geometry optimization. For the 2 × 1 × 1 and 2 × 2 × 1 supercells, *Γ*-centered 6 × 12 × 12 and 6 × 12 × 12 *k*-point grids were used, respectively. In the case of the 2 × 2 × 2 supercell, the

Monkhorst-Pack *k*-point mesh 6 × 6 × 6 was applied.³² The cut-off energy was 400 eV for all models. The optimization continued until the residual forces on the atoms became less than 0.5 meV Å⁻¹. The totally relaxed pristine and (co)substituted models were adopted for further calculations of the density of states (DOS) and band structures. To achieve the best agreement between experimental and theoretical results, the screened Coulomb hybrid HSE12s exchange-correlation functional was employed.⁴⁰ During the calculation of the DOS structure, *Γ*-centered 6 × 12 × 12, 4 × 4 × 8, and 3 × 3 × 3 *k*-point grids in the case of (co)substituted models within the 2 × 1 × 1, 2 × 2 × 1, and 2 × 2 × 2 supercells were applied, respectively. The Gaussian smearing method was used for the electronic structure calculations. The effective masses of electrons and holes were calculated using the Sumo-bandstats program through the parabolic fitting to the conduction band minimum (CBM) and valence band maximum (VBM).⁴¹ The band edge positions were calculated according to the empirical formula:^{42–45}

$$E_{\text{CB}} = \chi - E^{\text{e}} - 0.5 E_{\text{g}} \quad (1)$$

$$E_{\text{VB}} = E_{\text{CB}} - E_{\text{g}} \quad (2)$$

where E_{CB} and E_{VB} are the CB and VB edge potentials, respectively, E_{g} is the band gap. The Mulliken electronegativity of semiconductor χ can be calculated as the geometric mean of the absolute electronegativities of the constituent atoms. This is defined as the arithmetic mean of the electron affinities and atomic ionization. E^{e} is the energy of free electrons of the hydrogen scale (4.5 eV).^{46,47}

3. Results and discussion

Since doping can also influence the formation of a secondary phase depending on its concentration,⁴⁸ the crystal structure and purity of the synthesized samples were first analyzed by X-ray powder diffraction (XRD) analysis. The XRD patterns of pristine and (co)substituted samples are shown in Fig. 1. All reflections in the XRD patterns are identified as a single-phase cubic perovskite BaTaO₂N with the space group *Pm3̄m* (ICDD PDF 01-084-1748), and no reflections assignable to impurity phases are detected. In the perovskite structure of BaTaO₂N, Ba cations with a larger ionic radius occupy *A* site and has a 12-fold coordination, while Ta cations with a smaller ionic radius occupy a *B* site and have a 6-fold coordination at the octahedral sites. Since the ionic radii of Al³⁺ (53.5 pm) and Mg²⁺ (72 pm) substituents are closer to that of Ta⁵⁺ (64 pm) than that of Ba²⁺ (161 pm), both are expected to be (co)substituted for Ta⁵⁺. Apparently, the magnified XRD patterns indicate a slight alteration in the 2 θ angle position of the 110 reflection toward higher or lower 2 θ angles when Ta⁵⁺ is partially substituted by Al³⁺ (BT0N2) or Mg²⁺ (BT0N3) in the octahedral coordination, indicating the lattice volume contraction or expansion, respectively.³² As the ionic radius of Al³⁺ is smaller than that of Ta⁵⁺, while the ionic radius of Mg²⁺ is larger than that of Ta⁵⁺, the 2 θ angle position of the 110 reflections of the Al³⁺–





Fig. 1 X-Ray diffraction patterns of BTON1 (a), BTON2 (b), BTON3 (c), BTON4 (d), BTON5 (e), and BTON6 (f).

Mg^{2+} dual-substituted samples (BTON4-6) is near to that of pristine BaTaO_2N (BTON1). Also, the concurrent substitution of smaller O^{2-} (126 pm) for larger N^{3-} (157 pm) to compensate charge balance in the Al^{3+} - Mg^{2+} dual-substitution for Ta^{5+} may have lessened the lattice expansion.^{13,32} An opposite trend was observed when oxygen occupying the substitutional and interstitial lattice sites of $\text{K}_2\text{La}_2\text{Ti}_3\text{O}_{10}$ was intentionally substituted by nitrogen.⁴⁹ As the (co)substitution concentration is strictly controlled at 5%, no significant distortion in the crystal structure of BaTaO_2N is observed.

The photocatalytic water splitting activity of photocatalysts is greatly influenced by particle morphology, size, porosity, exposed facets, *etc.* Recently, it was found that the CoO_x cocatalyst could function more effectively in photoluminescence quenching and generating greater band bending on the {010} facet in dual-faceted BiVO_4 with respect to the {110} facet.⁵⁰ Also, the BaTaO_2N crystals with well-developed {111} facets²⁵ and coexposed anisotropic {100} and {110} facets²⁶ showed a significantly enhanced photocatalytic activity for H_2 evolution in comparison to the BaTaO_2N crystals with only

{100} facets. Thus, the microstructures of pristine and (co)substituted samples were also analyzed, and the SEM images are shown in Fig. 2. Pristine BaTaO_2N (BTON1) has irregular particles with an average size of 247 nm, and some particles contain pores (Fig. 2a). Evidently, the particle morphology and size were affected by changing the Al^{3+} - Mg^{2+} cosubstituent ratio. Namely, introducing 5% Al^{3+} (BTON2) significantly reduced the number of small particles, and large bulky particles with an average size of 338 nm and surface pores were formed (Fig. 2b). On one hand, these surface pores can, in principle, provide a large surface area that is beneficial for the photocatalytic water splitting reactions and also a greater number of dangling bonds that can act as nucleation centers for cocatalyst particles.²² On the other hand, they can also affect both charge transport within the photocatalyst and mass transfer of reactants and products, impacting the overall reaction kinetics.⁵¹ In Fig. 2c, the particle size was drastically decreased to an average size of 87 nm, and the particles became more joined with an intimate contact and without any surface pores after substituting 5% Mg^{2+} for Ta^{5+} (BTON3). When 2.5%

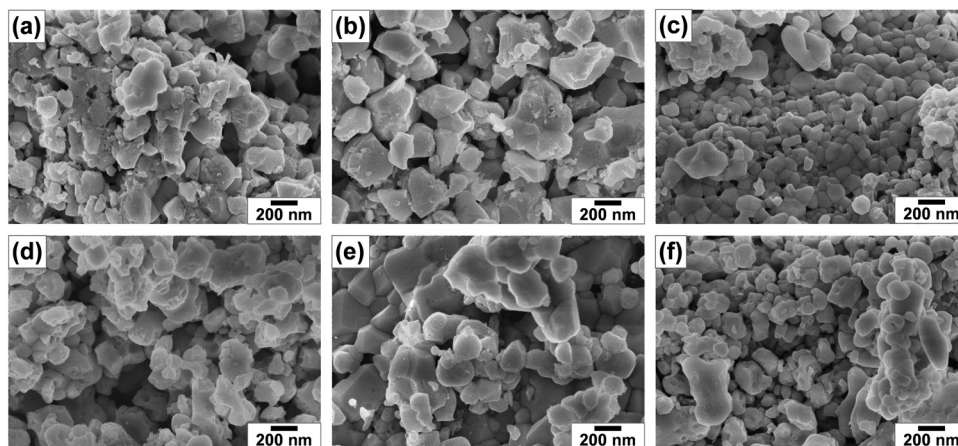


Fig. 2 SEM images of BTON1 (a), BTON2 (b), BTON3 (c), BTON4 (d), BTON5 (e), and BTON6 (f).

Al^{3+} and 2.5% Mg^{2+} (BTON4) were equally cosubstituted for Ta^{5+} (BTON4), the particles again became larger (285 nm) without a clear outline (Fig. 2d). When the $\text{Al}^{3+}:\text{Mg}^{2+}$ cosubstituent ratio was set to 3.5%:1.5% (BTON5), larger and denser crystals with idiomorphic shapes appeared along with smaller irregular particles with surface pores (Fig. 2e). In contrast, when the $\text{Al}^{3+}:\text{Mg}^{2+}$ cosubstituent ratio was adjusted to 1.5%:3.5% (BTON6), the average particle size was reduced to 93 nm (Fig. 2f). This indicates that the total interfacial free energy and kinetic factors were more substantially influenced by Mg^{2+} than Al^{3+} . In the previous study,³² the partial substitution of Mg^{2+} for Ta^{5+} in BaTaO_2N similarly reduced the number of plate-like particles and led to the formation of particles with idiomorphic shapes in comparison to other substituents. Furthermore, the solid-state reaction here induced the formation of more irregular particles despite $\text{Al}^{3+}\text{-Mg}^{2+}$ dual substitution in comparison to the flux method applied previously to synthesize BaTaO_2N particles,^{23,32,52} which may lead to the different photocatalytic activity. The EDX spectra of pristine and (co)substituted samples shown in Fig. S1 (ESI[†]) reveal the presence of Ba, Ta, O, N, Al, and Mg elements. The (co)substituent contents estimated by EDX and ICP-OES data are about 4.84% Al, 4.91% Mg, 2.42% Al + 2.38% Mg, 3.47% Al + 1.52% Mg, and 1.48% Al + 3.51% Mg for BTON2, BTON3, BTON4, BTON5, and BTON6, respectively, which are close to the nominal compositions of (co)substituents.

Fig. 3 shows the UV-Vis diffuse reflectance spectra of pristine and (co)substituted samples. Pristine BaTaO_2N (BTON1) has an optical absorption edge at 665 nm, corresponding to the optical bandgap energy of 1.86 eV. Obviously, the $\text{Al}^{3+}\text{-Mg}^{2+}$ cosubstituent ratio influenced visible-light absorption of BaTaO_2N . That is, the optical absorption edges of (co)substituted samples shifted toward shorter wavelengths, resulting in the optical bandgap energies of 1.90, 2.01, 1.96, 1.93, and 1.99 eV for BTON2, BTON3, BTON4, BTON5, and BTON6, respectively. Interestingly, increasing the concentration of Mg^{2+} led to a greater shift toward shorter wavelengths in comparison to that

of Al^{3+} . This is due to the substitution of more N^{3-} by O^{2-} to compensate charge balance in the $\text{Mg}^{2+}\text{-to-Ta}^{5+}$ substitution.^{13,32,34} The valence band of BaTaO_2N consists of hybridized N 2p and O 2p orbitals, and its position is affected by the N/O ratio as the N 2p orbitals are higher in energy than the O 2p orbitals. This is also reflected by the powder color of the synthesized samples shown in the insets of Fig. 3, where the higher the Mg^{2+} concentration, the brighter the powder color is. Although the $\text{Al}^{3+}\text{-Mg}^{2+}$ dual substitution induced a considerable blue-shift in light absorption, which is not beneficial in solar energy conversion, it is still advantageous in reducing the surface and bulk defects because of the suppression of Ta^{5+} reduction by $\text{Al}^{3+}/\text{Mg}^{2+}$ (co)substitution and altering the band edge positions with respect to water splitting potentials.⁵³

To probe the surface chemical composition and oxidation state of elements, X-ray photoelectron spectroscopy (XPS) measurements were conducted. In the XPS core-level spectra of Ta 4f in Fig. 4, the overlapping peaks of the Ta 4f_{5/2} and Ta 4f_{7/2} states of the Ta^{5+} species bonded to N^{3-} and O^{2-} can be deconvoluted into four different peaks centered at the binding energies of 25.70–26.16, 23.67–24.14, 27.07–27.11, and 25.01–26.09 eV, respectively.⁵⁴ Although there is no direct correlation between the intensities of the Ta(N) and Ta(O) peaks and $\text{Al}^{3+}\text{-Mg}^{2+}$ (co)substitution ratio, a slightly higher intensity in the Ta(O) peak can be observed in comparison to that of the Ta(N) peak when the $\text{Al}^{3+}:\text{Mg}^{2+}$ (co)substituent ratio is decreased because a large number of N^{3-} were substituted by O^{2-} to compensate charge balance in the $\text{Mg}^{2+}\text{-to-Ta}^{5+}$ substitution.^{13,32,34} No peaks associated with reduced tantalum species were noted as the partial substitution of Al^{3+} or/and Mg^{2+} suppressed the reduction of Ta^{5+} .⁵³ This leads to the reduction in the surface and bulk defects that can improve charge separation and photocatalytic activity.

Density functional theory (DFT) simulations were further involved to understand the electronic structures of pristine and (co)substituted BaTaO_2N models. First, the structural parameters of pristine and (co)substituted BaTaO_2N models were predicted by DFT-PBE. As shown in Table S1 (ESI[†]), the structural parameters of pristine BaTaO_2N model were found to be in good agreement with the experimental data reported previously.^{32,40} It can be noted that Al substitution leads to a contraction of lattice constants due to a smaller ionic radius of Al^{3+} (53.5 pm) than that of Ta^{5+} (64 pm). An opposite trend is observed in Mg substitution because the ionic radius of Mg^{2+} (72 pm) is larger than that of Ta^{5+} . The cosubstituted models can be characterized in the same manner depending on the Al and Mg contents. This is consistent with the X-ray diffraction data presented earlier.

Next, the effect of $\text{Al}^{3+}\text{-Mg}^{2+}$ (co)substitution at the Ta site in BaTaO_2N on electronic band structures was studied by DFT-HSE12s. As shown in Fig. 5, the estimated bandgap energy of pristine BaTaO_2N is 1.49 eV (direct-type), which is slightly lower than the experimentally^{32,55} and theoretically⁵⁶ obtained bandgap values due to the well-known underestimation. The calculation results reveal that the (co)substitution of Al and/or Mg at the Ta site in BaTaO_2N can generate acceptor states above the valence band maximum, shifting the valence band upward (Fig. 5).



Fig. 3 UV-Vis diffuse reflectance spectra of BTON1 (a), BTON2 (b), BTON3 (c), BTON4 (d), BTON5 (e), and BTON6 (f).





Fig. 4 Ta 4f high-resolution X-ray photoelectron spectra of BTON1 (a), BTON2 (b), BTON3 (c), BTON4 (d), BTON5 (e), and BTON6 (f).



Fig. 5 Electronic band structures of (a) BTON,³² (b) BTON:Al (50 at%), (c) BTON:Mg (50 at%), (d) BTON:Al:Mg (25:25 at%), (e) BTON:Al:Mg (37.5:12.5 at%), and (f) BTON:Al:Mg (12.5:37.5 at%). The Fermi level is set at 0 eV.

According to the density of states (DOS) plots, the distribution patterns of the atomic orbitals seem to be unchanged (Fig. S2, ESI[†]). The major contribution to the valence band comes from occupied O p and N p states, while the conduction band consists of empty Ta d

states. The dependence of the bandgap value on Al or/and Mg contents in pristine and (co)substituted BaTaO₂N models is shown in Fig. S3 (ESI[†]). Apparently, Al substitution results in a narrower bandgap value in comparison to Mg substitution. Meantime, three

cosubstituted models are characterized by a significant decrease in the band gap with an increase in the Al content, which is beneficial to absorb a significant fraction of visible light. Among the three cosubstituted models, the $\text{BaTa}_{0.5}\text{Al}_{0.375}\text{Mg}_{0.125}\text{O}_2\text{N}$ model has the narrowest band gap (1.36 eV).

The effective masses of electrons (m_e^*) and holes (m_h^*) were also estimated along specific directions (Table S2, ESI†). It is known that lower effective masses of charge carriers indicate their higher mobility, which is important for enhancing the photocatalytic activity.⁴⁵ In the case of pristine BaTaO_2N , the effective masses of electrons and holes are comparable and low. With Al and/or Mg (co)substitution, the effective masses of electrons become slightly lower than that in pristine BaTaO_2N , suggesting an improvement in the reduction ability of the (co)substituted BaTaO_2N models. A contrary tendency can be observed for the effective masses of holes, which increased three or more times as compared with that of pristine BaTaO_2N . The lowest effective masses of holes are noted for the $\text{BaTa}_{0.5}\text{Al}_{0.375}\text{Mg}_{0.125}\text{O}_2\text{N}$ model, which may exhibit its stronger oxidizing ability among (co)substituted compounds. Suitable redox potentials are also known as one of the major criteria for developing high-efficiency visible-light-active photocatalysts.^{45,46} As shown in Table S3 (ESI†), the calculated positions of the valence band maximum and conduction band minimum are aligned with respect to the normal hydrogen electrode (NHE), and Al^{3+} – Mg^{2+} (co)substituted BaTaO_2N photocatalysts can be promising candidates for visible-light-induced water splitting.

The effect of Al^{3+} – Mg^{2+} dual substitution on visible-light-induced photocatalytic activity of BaTaO_2N was investigated. The half-reaction time courses for the photocatalytic H_2 and O_2 evolution over pristine and (co)substituted BaTaO_2N samples are shown in Fig. 6. As shown in Fig. 6a, the quantity of evolved O_2 gradually increases in the following order within 5 hours of the photocatalytic reaction: $124.05 \mu\text{mol} < 171.4 \mu\text{mol} < 238.2 \mu\text{mol} < 271.5 \mu\text{mol} < 324.7 \mu\text{mol} < 406.2 \mu\text{mol}$ for BTON1, BTON2, BTON3, BTON5, BTON4, and BTON6, respectively. Clearly, compared with pristine BaTaO_2N (BTON1) and mono-substituted samples (BTON2 and BTON3), cosubstituted samples exhibit higher O_2 evolution, and the highest O_2

evolution ($406.2 \mu\text{mol}$) is observed for BTON6 with 1.5% Al^{3+} + 3.5% Mg^{2+} cosubstituents. It is argued that due to the decrement in the surface and bulk defects as a result of the partial replacement of Ta^{5+} by a higher number of Mg^{2+} in the Al^{3+} – Mg^{2+} dual substitution and altering the valence band position with respect to water oxidation potential. As shown in Fig. 6b, the highest quantity of evolved H_2 is obtained for BTON5 ($75.4 \mu\text{mol}$) followed by BTON4 ($60.5 \mu\text{mol}$), BTON6 ($51.9 \mu\text{mol}$), BTON2 ($45.4 \mu\text{mol}$), BTON3 ($31.7 \mu\text{mol}$), and BTON1 ($17.3 \mu\text{mol}$), respectively.

Kisch and Bahnemann⁵⁷ suggested that the comparison of photocatalyst performance must be done using the kinetic parameters extracted from experimental measurements performed using the same types of light source and reactor. Then, it is convenient to estimate the reaction rate in the initial stages as the respective slope of the O_2 and H_2 evolved vs. irradiation time plots. For the O_2 evolution, the reaction rates were estimated to be 178.66, 102.64, 79.33, 66.65, 55.89, and $31.44 \mu\text{mol h}^{-1}$ for BTON6, BTON4, BTON5, BTON3, BTON2, and BTON1, respectively. For the H_2 evolution, 18.94, 12.81, 8.34, 7.35, 3.93, and $1.78 \mu\text{mol h}^{-1}$ for BTON5, BTON4, BTON6, BTON2, BTON3, and BTON1, respectively. Clearly, BaTaO_2N modified with 1.48% Al + 3.51% Mg generated the highest quantity of O_2 ($178.66 \mu\text{mol h}^{-1}$) with an apparent quantum yield of 0.18% at 420 nm, and BaTaO_2N modified with 3.47% Al + 1.52% Mg produced the highest quantity of H_2 ($18.94 \mu\text{mol h}^{-1}$) with an apparent quantum yield of 0.64% at 420 nm. Considering that the variation of the specific surface area between the photocatalysts does not have a greater impact,⁵⁸ the trend observed in the initial reaction rate can be considered as evidence that reflects the improvement of the surface reactions due to the modification of the BaTaO_2N photocatalyst with Al^{3+} – Mg^{2+} dual substitution. In our recent work,³² the photocatalytic reaction rate of the cation-modified BaTaO_2N was correlated with the energy difference of the adsorbed intermediates, where the photocatalytic evolution of H_2 and O_2 was significantly enhanced using Al- and Mg-modified BaTaO_2N photocatalysts, respectively. Thus, it is argued that in the case of dual substitution of BaTaO_2N with



Fig. 6 Reaction time courses for photocatalytic O_2 (a) and H_2 (b) evolution over BTON1, BTON2, BTON3, BTON4, BTON5, and BTON6 loaded with CoO_x and Pt nanoparticles as O_2 and H_2 evolution cocatalysts under visible light irradiation.



Al^{3+} and Mg^{2+} , the photocatalytic performance to form H_2 can be favored in the photocatalyst with a higher proportion of Al^{3+} . Regarding the evolution of O_2 , it was reported that the modification with Mg^{2+} presented a higher reaction rate than the undoped BTON and the Al-doped BTON.³² The latter suggests that the highest reactivity for the evolution of O_2 can be achieved with the photocatalyst having the highest percentage of Mg^{2+} . Therefore, the Al^{3+} – Mg^{2+} dual substitution can modulate the photocatalytic activity of BaTaO_2N .

The Al^{3+} – Mg^{2+} dual substitution in BaTaO_2N leads to the improvement in the kinetics of photocatalytic processes as a result of efficient electron transfer and the reduction of recombination processes. The interrelation of both phenomena (electron transfer and recombination) in BaTaO_2N photocatalysts has been discussed in previous works,^{13,20,23} and the optoelectronic properties were presented to be responsible for the changes in the photocatalytic behavior. For instance, the codoping of Ta_3N_5 with Mg and Zr¹³ and the modification of BaTaO_2N with Ca and cobalt oxide¹⁷ significantly affected the optoelectronic properties in such a way that the co-doped photocatalysts could exhibit the lower onset potentials and higher photocatalytic activity for photoelectrochemical water splitting. Modification of BaTaO_2N and LaTiO_2N with Zn and Ca has also been shown to significantly influence carrier density, to shift the band edge position, and to improve the yield of photo-redox reactions.³³ Similar results have been reported in BaTaO_2N with various dopants.^{31,34}

For Al^{3+} – Mg^{2+} -(co)substituted BaTaO_2N , the photocatalytic performance observed for the evolution of O_2 and H_2 (Fig. 6), the changes in visible light absorption (Fig. 3), and DFT calculations (Fig. 5) support the alteration in the electronic states of the photocatalyst with Al^{3+} and/or Mg^{2+} . Therefore, the difference in the dynamics of charge carriers affected the photocatalytic performance of pristine and (co)substituted photocatalysts. The relevance of DFT calculations to detect band structure effects that correlate with photocatalytic activity is convenient. Using the DFT calculations, Ni *et al.*⁵⁹ estimated the changes in the electronic structure of ZnSe by co-substitution of Sb at Se sites and Sc or Y at Zn sites, suggesting the importance of the effect of strong Coulombic interactions. It was also noted that the dual substitution resulted in a reduced bandgap, absorption in visible light, and energetic position of the bands relative to the redox potentials of water. By applying the DFT calculations, the role of F and N in the co-doped TiO_2 was studied,⁶⁰ indicating that the co-substitution of foreign atoms affects the band structure and provides new pathways for the appearance of different physicochemical processes (*e.g.*, enhanced adsorption of reagents, formation of new bonds, changes in the band structure, *etc.*) that provide improvements to the photocatalytic activity. As the dynamics of charge carriers is defined by the electronic structure, the DFT results presented here for BaTaO_2N cosubstituted with Al^{3+} and Mg^{2+} (Fig. 5) allow to assertively detect those changes in the electronic band structure that could have effects and/or be related to the performance of the photocatalysts. Further, the effect of Al^{3+} – Mg^{2+} dual substitution on surface property

(water and methanol adsorption) of BaTaO_2N is also theoretically explored.

Along with other factors, the adsorption of water molecules and formed intermediates on the photocatalyst surface has a strong influence on photocatalytic activity. In our recent work, the experimental photocatalytic reaction rates of pristine and cation-doped BaTaO_2N surfaces terminated with TaO_6 , TaN_6 , and TaO_4N_2 were well presented using the adsorption energies of intermediates (H^* for H_2 evolution and HO^* and O^* for O_2 evolution) estimated by molecular dynamics calculations.³² Another study has shown that the nickel modification can improve the adsorption of water molecules on anatase- TiO_2 , rutile- TiO_2 , and ZnO photoanodes, enhancing their photoelectrochemical performance.⁶¹ Particularly, Adsorption Locator for modelling has been broadly used for evaluating the adsorption interaction or non-bonded energies of organic and water molecules for various applications, including biomolecule/surface interactions,⁶² adsorption of SiF_4 and HF gaseous molecules at the molecular level,⁶³ next-generation protein-based biosensor surfaces,⁶⁴ catalyst/adsorbents for oil recovery and viscosity reduction process,⁶⁵ drug delivery tool in biological systems,⁶⁶ *etc.* Here, the influence of the Al^{3+} – Mg^{2+} dual



Fig. 7 Water and methanol molecules and field density distribution on the $\text{BaTaO}_2\text{N}(110)$ surfaces with 5% Al (a), 2.5% Al and 2.5% Mg (b), and 5% Mg (c). Atoms: grey – hydrogen, red – oxygen, blue – nitrogen, yellow – magnesium, pink – aluminum, light blue – tantalum, green – barium; Isosurface: red – methanol, green – water.



substitution on the adsorption of water molecules on the BaTaO₂N(110) surfaces was also explored by combined Molecular Dynamics and Monte-Carlo computer simulation. The Forcite and Adsorption Locator modules in BIOVIA Materials Studio 2017 software⁶⁷ was used to determine the most favorable adsorption sites and to evaluate the adsorption energy of water molecules on the BaTaO₂N(110) surfaces at different concentrations of the Al³⁺ and Mg²⁺ (co)substituents (Table S5, ESI†). The simulation data reveal that the adsorption energies of water molecules increase linearly by the Al³⁺-for-Ta⁵⁺ substitution on the BaTaO₂N(110) surface. The simultaneous adsorption of water and methanol molecules is higher than the adsorption of only water molecules (Fig. S4, ESI†), which increases depending on the Al³⁺ content. The differential adsorption (dE_{ads}/dN_i) of water molecules in water or water-methanol systems on the BaTaO₂N(110) surfaces have similar values (2.3–2.7 kcal mol⁻¹). The methanol molecules interact more strongly with Al³⁺-Mg²⁺-cosubstituted surfaces (4.95–6.14 kcal mol⁻¹). Fig. 7 shows close contacts between water molecules and Al³⁺-, Mg²⁺- and Al³⁺-Mg²⁺-(co)substituted BaTaO₂N(110) surfaces. However, methanol molecules tend to interact better with magnesium atoms on the BaTaO₂N(110) surface. Thus, compared with Al³⁺- or Mg²⁺ substitution, the Al³⁺-Mg²⁺ dual substitution can improve the adsorption of water and methanol molecules on the surface of BaTaO₂N, enhancing its photocatalytic activity.

4. Conclusions

In summary, the partial Al³⁺-Mg²⁺ dual substitution (5%) was applied to engineer structural defects and to modulate optoelectronic, surface, and photocatalytic activity of BaTaO₂N. The optical absorption edge of BaTaO₂N was shifted to shorter wavelengths after (co)substitution of Al³⁺ and/or Mg²⁺ for Ta⁵⁺, leading to the increase in the optical bandgap energy. This effect was more pronounced in the samples with higher content of Mg²⁺ because a large number of O²⁻ were substituted for N³⁻ to compensate charge balance. Similarly, a partial substitution of Mg²⁺ for Ta⁵⁺ affected the morphology of BaTaO₂N particles in comparison to Al³⁺, reducing the average particle size significantly. The initial reaction rates for the evolution of O₂ and H₂ revealed the improvement in the photocatalytic performance of BaTaO₂N photocatalysts due to Al³⁺-Mg²⁺ dual substitution. Particularly, BaTaO₂N modified with 1.48% Al + 3.51% Mg generated the highest quantity of O₂ (178.66 μmol h⁻¹) and exhibited an apparent quantum yield of 0.18% at 420 nm, while BaTaO₂N modified with 3.47% Al + 1.52% Mg produced the highest quantity of H₂ (18.94 μmol h⁻¹) and exhibited an apparent quantum yield of 0.64% at 420 nm. This enhancement in the photocatalytic O₂ and H₂ evolution over Al³⁺-Mg²⁺-(co)substituted BaTaO₂N photocatalysts can be related to the changes in the defect density, dynamics of charge carriers, electronic band structure, improvement in water and methanol adsorption, and favorable shift in the band energy levels with respect to water reduction and oxidation potentials.

Conflicts of interest

There are no conflicts to declare.

Acknowledgements

The authors would like to thank Dr Ina Remy-Speckmann, Dipl. Phys. Christoph Fahrenson, Ms Reiko Shiozawa, and Dr Aleksei G. Krasnov for their kind assistance in XRD, SEM-EDX and XPS analyses and DFT calculations, respectively. This project received funding from the European Union's Horizon 2020 Research and Innovation Programme under the Marie Skłodowska-Curie grant agreement no. 793882.

References

- Q. Wang and K. Domen, Particulate Photocatalysts for Light-Driven Water Splitting: Mechanisms, Challenges, and Design Strategies, *Chem. Rev.*, 2020, **120**, 919–985.
- T. Takata and K. Domen, Defect engineering of photocatalysts by doping of aliovalent metal cations for efficient water splitting, *J. Phys. Chem. C*, 2009, **113**, 19386–19388.
- W. J. Jo, H. J. Kang, K.-J. Kong, Y. S. Lee, H. Park, Y. Lee, T. Buonassisi, K. K. Gleason and J. S. Lee, Phase transition-induced band edge engineering of BiVO₄ to split pure water under visible light, *Proc. Natl. Acad. Sci. U. S. A.*, 2015, **112**, 13774–13778.
- M. Tayebi and B.-K. Lee, The effects of W/Mo-co-doped BiVO₄ photoanodes for improving photoelectrochemical water splitting performance, *Catal. Today*, 2021, **361**, 183–190.
- J. Xiao, B. Du, S. Hu, J. Zhong, X. Chen, Y. Zhang, D. Cai, S.-F. Zhou and G. Zhan, Simultaneously Enhanced Charge Separation and Transfer in Cocatalyst-Free Hematite Photoanode by Mo/Sn Codoping, *ACS Appl. Energy Mater.*, 2021, **4**, 10368–10379.
- T. J. Smart, V. U. Baltazar, M. Chen, B. Yao, K. Mayford, F. Bridges, Y. Li and Y. Ping, Doping Bottleneck in Hematite: Multipole Clustering by Small Polarons, *Chem. Mater.*, 2021, **33**, 4390–4398.
- Q. Wang, T. Hisatomi, S. S. K. Ma, Y. Li and K. Domen, Core/Shell Structured La- and Rh-Codoped SrTiO₃ as a Hydrogen Evolution Photocatalyst in Z-Scheme Overall Water Splitting under Visible Light Irradiation, *Chem. Mater.*, 2014, **26**, 4144–4150.
- Y. Qin, F. Fang, Z. Xie, H. Lin, K. Zhang, X. Yu and K. Chang, La,Al-Codoped SrTiO₃ as a Photocatalyst in Overall Water Splitting: Significant Surface Engineering Effects on Defect Engineering, *ACS Catal.*, 2021, **11**, 11429–11439.
- X. Sun, Y. Mi, F. Jiao and X. Xu, Activating Layered Perovskite Compound Sr₂TiO₄ via La/N Codoping for Visible Light Photocatalytic Water Splitting, *ACS Catal.*, 2018, **8**, 3209–3221.
- A. Iwase, K. Saito and A. Kudo, Sensitization of NaMO₃ (M: Nb and Ta) Photocatalysts with Wide Band Gaps to Visible Light by Ir Doping, *Bull. Chem. Soc. Jpn.*, 2009, **82**, 514–518.



- 11 A. Iwase and A. Kudo, Development of Ir and La-codoped BaTa₂O₆ photocatalysts using visible light up to 640 nm as an H₂-evolving photocatalyst for Z-schematic water splitting, *Chem. Commun.*, 2017, **53**, 6156–6159.
- 12 A. Iwase and H. Misono, Development of visible-light-responsive Ir and La-codoped KTaO₃ photocatalysts for water splitting, *Chem. Commun.*, 2021, **57**, 10331–10334.
- 13 J. Seo, T. Takata, M. Nakabayashi, T. Hisatomi, N. Shibata, T. Minegishi and K. Domen, Mg–Zr Cosubstituted Ta₃N₅ Photoanode for Lower-Onset-Potential Solar-Driven Photoelectrochemical Water Splitting, *J. Am. Chem. Soc.*, 2015, **137**, 12780–12783.
- 14 J. Xiao, J. J. M. Vequizo, T. Hisatomi, J. Rabeah, M. Nakabayashi, Z. Wang, Q. Xiao, H. Li, Z. Pan, M. Krause, N. Yin, G. Smith, N. Shibata, A. Brückner, A. Yamakata, T. Takata and K. Domen, Simultaneously Tuning the Defects and Surface Properties of Ta₃N₅ Nanoparticles by Mg–Zr Codoping for Significantly Accelerated Photocatalytic H₂ Evolution, *J. Am. Chem. Soc.*, 2021, **143**, 10059–10064.
- 15 M. Higashi, R. Abe, K. Teramura, T. Takata, B. Ohtani and K. Domen, Two step water splitting into H₂ and O₂ under visible light by ATaO₂N (A = Ca, Sr, Ba) and WO₃ with IO₃[−]/I[−] shuttle redox mediator, *Chem. Phys. Lett.*, 2008, **452**, 120–123.
- 16 K. Maeda and K. Domen, Water Oxidation Using a Particulate BaZrO₃-BaTaO₂N Solid-Solution Photocatalyst That Operates under a Wide Range of Visible Light, *Angew. Chem., Int. Ed.*, 2012, **51**, 9865–9869.
- 17 S. Wei, G. Zhang and X. Xu, Activating BaTaO₂N by Ca modifications and cobalt oxide for visible light photocatalytic water oxidation reactions, *Appl. Catal., B*, 2018, **237**, 373–381.
- 18 Z. Wang, Y. Luo, T. Hisatomi, J. J. M. Vequizo, S. Suzuki, S. Chen, M. Nakabayashi, L. Lin, Z. Pan, N. Kariya, A. Yamakata, N. Shibata, T. Takata, K. Teshima and K. Domen, Sequential cocatalyst decoration on BaTaO₂N towards highly-active Z-scheme water splitting, *Nat. Commun.*, 2021, **12**, 1005.
- 19 S. Jadhav, S. Hasegawa, T. Hisatomi, Z. Wang, J. Seo, T. Higashi, M. Katayama, T. Minegishi, T. Takata, J. M. Peralta-Hernández, O. S. Torres and K. Domen, Efficient photocatalytic oxygen evolution using BaTaO₂N obtained from nitridation of perovskite-type oxide, *J. Mater. Chem. A*, 2020, **8**, 1127–1130.
- 20 J. Seo, M. Nakabayashi, T. Hisatomi, N. Shibata, T. Minegishi and K. Domen, Solar-Driven Water Splitting over a BaTaO₂N Photoanode Enhanced by Annealing in Argon, *ACS Appl. Energy Mater.*, 2019, **2**, 5777–5784.
- 21 M. Hojamberdiev, K. Yubuta, J. J. M. Vequizo, A. Yamakata, S. Oishi, K. Domen and K. Teshima, NH₃-Assisted Flux Growth of Cube-like BaTaO₂N Submicron Crystals in a Completely Ionized Nonaqueous High-Temperature Solution and Their Water Splitting Activity, *Cryst. Growth Des.*, 2015, **15**, 4663–4671.
- 22 M. Hojamberdiev, K. Kawashima, T. Hisatomi, M. Katayama, M. Hasegawa, K. Domen and K. Teshima, Distinguishing the effects of altered morphology and size on the visible light-induced water oxidation activity and photoelectrochemical performance of BaTaO₂N crystal structures, *Faraday Discuss.*, 2019, **215**, 227–241.
- 23 M. Hojamberdiev, J. M. Mora-Hernandez, R. Vargas, A. Yamakata, K. Yubuta, E. M. Heppke, L. M. Torres-Martínez, K. Teshima and M. Lerch, Time-Retrenched Synthesis of BaTaO₂N by Localizing an NH₃ Delivery System for Visible-Light-Driven Photoelectrochemical Water Oxidation at Neutral pH: Solid-State Reaction or Flux Method?, *ACS Appl. Energy Mater.*, 2021, **4**, 9315–9327.
- 24 K. Teshima, Y. Hara, K. Yubuta, S. Oishi, K. Domen and M. Hojamberdiev, Application of Flux Method to the Fabrication of Ba₅Ta₄O₁₅, Sr₅Ta₄O₁₅, Sr₂Ta₂O₇, and BaTaO₂N Polycrystalline Films on Ta Substrates, *Cryst. Growth Des.*, 2017, **17**, 1583–1588.
- 25 Y. Luo, Z. Wang, T. Yamada, K. Yubuta, S. Suzuki, T. Hisatomi, K. Domen and K. Teshima, Platy BaTaO₂N Crystals Fabricated from K₂CO₃-KCl Binary Flux for Photocatalytic H₂ Evolution, *ACS Appl. Energy Mater.*, 2020, **3**, 10669–10675.
- 26 Y. Luo, S. Suzuki, Z. Wang, K. Yubuta, J. J. M. Vequizo, A. Yamakata, H. Shiiba, T. Hisatomi, K. Domen and K. Teshima, Construction of Spatial Charge Separation Facets on BaTaO₂N Crystals by Flux Growth Approach for Visible-Light-Driven H₂ Production, *ACS Appl. Mater. Interfaces*, 2019, **11**, 22264–22271.
- 27 K. Hibino, M. Yashima, T. Oshima, K. Fujii and K. Maeda, Structures, electron density and characterization of novel photocatalysts, (BaTaO₂N)_{1−x}(SrWO₃N)_x solid solutions, *Dalton Trans.*, 2017, **46**, 14947–14956.
- 28 Z. Lan, T. Vegge and I. E. Castelli, Theoretical Insight on Anion Ordering, Strain, and Doping Engineering of the Oxygen Evolution Reaction in BaTaO₂N, *Chem. Mater.*, 2021, **33**, 3297–3303.
- 29 K. Ueda, T. Minegishi, J. Clune, M. Nakabayashi, T. Hisatomi, H. Nishiyama, M. Katayama, N. Shibata, J. Kubota, T. Yamada and K. Domen, Photoelectrochemical Oxidation of Water Using BaTaO₂N Photoanodes Prepared by Particle Transfer Method, *J. Am. Chem. Soc.*, 2015, **137**, 2227–2230.
- 30 T. Takata and K. Domen, Defect Engineering of Photocatalysts by Doping of Aliovalent Metal Cations for Efficient Water Splitting, *J. Phys. Chem. C*, 2009, **113**, 19386–19388.
- 31 M. Higashi, Y. Yamanaka, O. Tomita and R. Abe, Fabrication of Cation-Doped BaTaO₂N Photoanodes for Efficient Photoelectrochemical Water Splitting Under Visible Light Irradiation, *APL Mater.*, 2015, **3**, 104418.
- 32 M. Hojamberdiev, R. Vargas, Z. C. Kadirova, K. Kato, H. Sena, A. G. Krasnov, A. Yamakata, K. Teshima and M. Lerch, Unfolding the Role of B Site-Selective Doping of Aliovalent Cations on Enhancing Sacrificial Visible Light-Induced Photocatalytic H₂ and O₂ Evolution over BaTaO₂N, *ACS Catal.*, 2022, **12**, 1403–1414.
- 33 Y. Bao, H. Zou, N. Yang, G. Li and F. Zhang, Synthesis of perovskite BaTaO₂N with low defect by Zn doping for boosted photocatalytic water reduction, *J. Energy Chem.*, 2021, **63**, 358–363.



- 34 H. Zhang, S. Wei and X. Xu, Mg modified BaTaO₂N as an efficient visible-light-active photocatalyst for water oxidation, *J. Catal.*, 2020, **383**, 135–143.
- 35 K. Maeda, D. Lu and K. Domen, Oxidation of Water under Visible-Light Irradiation over Modified BaTaO₂N Photocatalysts Promoted by Tungsten Species, *Angew. Chem., Int. Ed.*, 2013, **52**, 6488–6491.
- 36 G. Kresse and J. Furthmüller, Efficient iterative schemes for ab initio total-energy calculations using a plane-wave basis set, *Phys. Rev. B: Condens. Matter Mater. Phys.*, 1996, **54**, 11169–11186.
- 37 D. Joubert, From ultrasoft pseudopotentials to the projector augmented-wave method, *Phys. Rev. B: Condens. Matter Mater. Phys.*, 1999, **59**, 1758–1775.
- 38 F. Pors, R. Marchand, Y. Laurent, P. Bacher and G. Roult, Etude structurale des perovskites oxyazotées BaTaO₂N et BaNbO₂N. Structural study of BaTaO₂N and BaNbO₂N oxynitrided perovskites, *Mater. Res. Bull.*, 1988, **23**, 1447–1450.
- 39 J. P. Perdew, K. Burke and M. Ernzerhof, Generalized gradient approximation made simple, *Phys. Rev. Lett.*, 1996, **77**, 3865–3868.
- 40 J. E. Moussa, P. A. Schultz and J. R. Chelikowsky, Analysis of the Heyd-Scuseria-Ernzerhof density functional parameter space, *J. Chem. Phys.*, 2012, **136**, 1–11.
- 41 A. M. Ganose, A. J. Jackson and D. O. Scanlon, Sumo: Command-Line Tools for Plotting and Analysis of Periodic Ab Initio Calculations, *J. Open Source Softw.*, 2018, **3**, 717.
- 42 M. Hojamberdiev, E. Zahedi, E. Nurlaela, K. Kawashima, K. Yubuta, M. Nakayama, H. Wagata, T. Minegishi, K. Domen and K. Teshima, The Cross-Substitution Effect of Tantalum on the Visible-Light-Driven Water Oxidation Activity of BaNbO₂N Crystals Grown Directly by an NH₃-Assisted Flux Method, *J. Mater. Chem. A*, 2016, **4**, 12807–12817.
- 43 Z. Ma, Z. Yi, J. Sun and K. Wu, Electronic and Photocatalytic Properties of Ag₃PC₄^{VI} (C=O, S, Se): A Systemic Hybrid DFT Study, *J. Phys. Chem. C*, 2012, **116**, 25074–25080.
- 44 A. G. Krasnov, M. S. Napalkov, M. I. Vlasov, M. S. Koroleva, I. R. Shein and I. V. Piir, Photocatalytic Properties of Bi_{2–x}Ti₂O_{7–1.5x} (x = 0, 0.5) Pyrochlores: Hybrid DFT Calculations and Experimental Study, *Inorg. Chem.*, 2020, **59**, 12385–12396.
- 45 M. A. Butler and D. S. Ginley, Prediction of Flatband Potentials at Semiconductor-Electrolyte Interfaces from Atomic Electronegativities, *J. Electrochem. Soc.*, 1978, **125**, 228–232.
- 46 M. Benčina, M. Valant and M. Ben, Bi₂Ti₂O₇-Based Pyrochlore Nanoparticles and Their Superior Photocatalytic Activity under Visible Light, *J. Am. Ceram. Soc.*, 2018, **101**, 82–90.
- 47 H. Sameie, A. A. Sabbagh Alvani, N. Naseri, S. Du and F. Rosei, First-Principles Study on ZnV₂O₆ and Zn₂V₂O₇: Two New Photoanode Candidates for Photoelectrochemical Water Oxidation, *Ceram. Int.*, 2018, **44**, 6607–6613.
- 48 K. Kawashima, M. Hojamberdiev, H. Wagata, M. Nakayama, K. Yubuta, S. Oishi, K. Domen and K. Teshima, Amount of tungsten dopant influencing the photocatalytic water oxidation activity of LaTiO₂N crystals grown directly by an NH₃-assisted flux method, *Catal. Sci. Technol.*, 2016, **6**, 5389–5396.
- 49 K. Kawashima, M. Hojamberdiev, H. Wagata, K. Yubuta, K. Domen and K. Teshima, Protonated Oxide, Nitrided, and Reoxidized K₂La₂Ti₃O₁₀ Crystals: Visible-Light-Induced Photocatalytic Water Oxidation and Fabrication of Their Nanosheets, *ACS Sustainable Chem. Eng.*, 2017, **5**, 232–240.
- 50 Z. Xie, H. L. Tan, H. Wu, R. Amal, J. Scott and Y. H. Ng, Facet-dependent Spatial Charge Separation with Rational Co-catalyst Deposition on BiVO₄, *Mater. Today Energy*, 2022, **26**, 100986.
- 51 M. Zbiri, C. M. Aitchison, R. S. Sprick, A. I. Cooper and A. A. Y. Guilbert, Probing Dynamics of Water Mass Transfer in Organic Porous Photocatalyst Water-Splitting Materials by Neutron Spectroscopy, *Chem. Mater.*, 2021, **33**, 1363–1372.
- 52 M. Hojamberdiev and K. Kawashima, Exploring flux-grown transition metal oxynitride perovskites for photocatalytic water oxidation: A minireview, *Energy Rep.*, 2020, **6**, 13–24.
- 53 J. Seo, D. Ishizuka, T. Hisatomi, T. Takata and K. Domen, Effect of Mg²⁺ substitution on the photocatalytic water splitting activity of LaMg_xNb_{1–x}O_{1+3x}N_{2–3x}, *J. Mater. Chem. A*, 2021, **9**, 8655–8662.
- 54 C. Wang, T. Hisatomi, T. Minegishi, Q. Wang, M. Zhong, M. Katayama, J. Kubota and K. Domen, Synthesis of Nanostructured BaTaO₂N Thin Films as Photoanodes for Solar Water Splitting, *J. Phys. Chem. C*, 2016, **120**, 15758–15764.
- 55 K. Kawashima, M. Hojamberdiev, K. Yubuta, K. Domen and K. Teshima, Synthesis and Visible-Light-Induced Sacrificial Photocatalytic Water Oxidation of Quinary Oxynitride BaNb_{0.5}Ta_{0.5}O₂N Crystals, *J. Energy Chem.*, 2018, **27**, 1415–1421.
- 56 X. Xu and H. Jiang, First-Principles Investigation on Anion Order, Electronic Structure and Dielectric Properties of BaTaO₂N, *J. Mater. Chem. A*, 2019, **7**, 14583–14591.
- 57 H. Kisch and D. Bahnemann, Best practice in photocatalysis: Comparing rates or apparent quantum yields, *J. Phys. Chem. Lett.*, 2015, **6**, 1907–1910.
- 58 F. Wu, G. Liu and X. Xu, Efficient photocatalytic oxygen production over Ca-modified LaTiO₂N, *J. Catal.*, 2017, **346**, 10–20.
- 59 C. Ni, C. Fu, B. Wang, H. Yuan and H. Chen, Charge-compensated codoped pseudohexagonal zinc selenide nanosheets towards enhanced visible-light-driven photocatalytic water splitting for hydrogen production, *Int. J. Hydrogen Energy*, 2021, **46**, 34305–34317.
- 60 A. Miyoshi, A. Kuwabara and K. Maeda, Effects of Nitrogen/Fluorine Codoping on Photocatalytic Rutile TiO₂ Crystal Studied by First-Principles Calculations, *Inorg. Chem.*, 2021, **60**, 2381–2389.
- 61 M. Hojamberdiev, R. Vargas, V. S. Bhati, D. Torres, Z. C. Kadirova and M. Kumar, Unraveling the photoelectrochemical behavior of Ni-modified ZnO and TiO₂ thin films fabricated by RF magnetron sputtering, *J. Electroanal. Chem.*, 2021, **882**, 115009.
- 62 S. Galvez-Martinez, E. Escamilla-Roa, M. P. Zorzano and E. Mateo-Marti, Defects on a pyrite (100) surface produce chemical evolution of glycine under inert conditions: experimental and theoretical approaches, *Phys. Chem. Chem. Phys.*, 2019, **21**, 24535–24542.



- 63 M. Khnifira, A. Mahsoun, M. E. Belghiti, L. Khamar, M. Sadiq, M. Abdenouni and N. Barka, HF and SiF₄ adsorption on carbon graphite (111) surface in aqueous medium: A combined DFT and MD simulation approach, *Mater. Today: Proc.*, 2021, **37**, 3987–3993.
- 64 J. S. Cross, Y. Kubota, A. Chatterjee, S. Unni, T. Ikoma and M. Tagaya, Interfacial Modeling of Fibrinogen Adsorption onto LiNbO₃ Single Crystal-Single Domain Surfaces, *Int. J. Mol. Sci.*, 2021, **22**, 5946.
- 65 T. Montoya, A. Amrollahi, G. Vitale, N. Hosseinpour and N. N. Nassar, Size Effects of NiO Nanoparticles on the Competitive Adsorption of Quinolin-65 and Violanthrone-79: Implications for Oil Upgrading and Recovery, *ACS Appl. Nano Mater.*, 2020, **3**, 5311–5326.
- 66 E. A. Abdullah, Theoretical study of a single-walled carbon nanotube and a cellulose biofiber as 5-fluorouracil anti-cancer drug carriers, *Eur. J. Chem.*, 2022, **13**, 69–77.
- 67 S. Sharma, P. Kumar and R. Chandra, Applications of BIOVIA Materials Studio, LAMMPS, and GROMACS in Various Fields of Science and Engineering, in *Molecular Dynamics Simulation of Nanocomposites Using BIOVIA Materials Studio, Lammmps and Gromacs*, ed. S. Sharma, 2019, pp. 329–341.

